ROYAL SOCIETY
OF **CHEMISTRY**

PAPER
Fumiaki Amano *et al.*
Gas-fed photoelectrochemical reactions sustained by
phosphotungstic acid as an inorganic surface electrolyte

PAPER

Gas-fed photoelectrochemical reactions sustained by phosphotungstic acid as an inorganic surface electrolyte†

Fumiaki Amano, (iD) *[a] Keisuke Tsushiro[ab] and Chiho Akamoto[b]

Gas-fed photoelectrochemical (PEC) system with a porous photoelectrode and proton-exchange membrane (PEM) has the potential to produce hydrogen from water vapour and activate methane at room temperature. To effectively drive gas-phase PEM-PEC reactions, porous photoelectrodes should be coated with a solid electrolyte of perfluorinated sulfonic acid (PFSA) ionomers. However, fluorocarbon-based ionomers were not chemically stable in vapour-fed PEC systems. Herein, we report that polyoxometalate, an inorganic proton-conducting material, may be employed as the surface electrolyte of a WO_3 porous photoelectrode for vapour-fed water splitting and methane activation under visible light irradiation. We demonstrate that the porous WO_3 photoanode modified with phosphotungstic acid ($H_3PW_{12}O_{40}$) induces PEC reactions, including the oxygen evolution reaction and methane conversion, under gas feeding. Additionally, we demonstrated improved durability by using the inorganic surface electrolyte.

Introduction

Photoelectrochemical (PEC) water splitting is a method of producing hydrogen using renewable energy with no carbon dioxide emissions. Water vapour harvesting from ambient humidity may solve the freshwater shortage problem in the world, making green H_2 sustainable.[1–3] The use of water vapour has the additional benefit of minimizing active water purification, liquid pumping, and bubble formation.[4–6] The gas-fed PEM-PEC reactions for producing H_2 necessitate the use of all-solid PEC devices with polymer electrolyte membranes that operate at low temperatures around 25 °C.

Prototype gas-fed PEC systems have been developed using a proton exchange membrane (PEM) with a porous photoanode and cathode electrocatalyst.[7–23] We found that the surface coating of the porous photoelectrodes with perfluorinated sulfonic acid (PFSA) ionomers significantly enhanced the PEC performance of the vapour-fed system operating without liquid electrolyte.[13–17] The surface ionomer decorated on the porous photoanodes forms a triple-phase boundary, allowing gas, semiconductor particles, and electrolyte to come into contact simultaneously, facilitating proton-coupled electron transfer

(PCET) and charge transport in the gas-fed PEC cell. Surface proton conduction is promoted by the humidity-adsorbed water layer in the ionomer.[16,19,20,22]

Surface coatings of the PFSA ionomers, such as Nafion® from Chemours and Aquivion® from Solvay, aid in PCET and proton transport in the functionalized porous photoelectrode.[11,13–17,22,23] As a result, PFSA-functionalized photoanodes such as TiO_2 and $SrTiO_3$ can induce vapour-fed water splitting with as high efficiency as the conventional liquid electrolyte system.[14–16] The all-solid PEM-PEC system using porous photoanodes such as TiO_2 and WO_3 has also been employed in the CH_4 conversion reactions (steam reforming of methane and dehydrogenative coupling to ethane).[24,25] The selectivity for C_2H_6 from CH_4 was more than 50% on a carbon basis for the ionomer-coated WO_3 photoanode under visible light irradiation.

However, the photocurrent responses in the PEM-PEC cells gradually decreased with the accompanying CO_2 formation during vapour-fed water splitting reactions under UV irradiation.[14–16,22] This degradation suggests oxidative decomposition of the PFSA ionomers decorated on the photoanode surface by the photogenerated holes and hydroxyl radicals. Although the fluorocarbon backbones are chemically stable compared with other organic materials, PFSA ionomers are degraded by hydroxyl radicals during PEM fuel cell operation.[26] In the same way, the PFSA ionomer decorated on the photoanodes would be oxidized by the valence band holes and the photogenerated hydroxyl radical in the PEM-PEC system.

[a] Department of Applied Chemistry for Environment, Tokyo Metropolitan University, 1-1 Minami-Osawa, Hachioji, Tokyo 192-0397, Japan. E-mail: f.amano@tmu.ac.jp
[b] Department of Chemical and Environmental Engineering, The University of Kitakyushu, 1-1 Hibikino, Wakamatsu-ku, Kitakyushu, Fukuoka 808-0135, Japan
† Electronic supplementary information (ESI) available. See DOI: https://doi.org/10.1039/d3ya00568b

To avoid the degradation of the triple-phase boundary in the functionalized photoanodes, we explored polyoxometalate, an inorganic proton-conducting material that is oxidatively stable in comparison with other organic materials, as a surface electrolyte to replace the PFSA ionomer. In this study, we studied the surface modification of a porous WO_3 photoanode with phosphotungstic acid (PWA) to improve the photocurrent response in water vapour splitting and CH_4 conversion reactions in a gas-fed PEM-PEC system. PWA ($H_3PW_{12}O_{40}$) is a polyoxometalate with Brønsted acidity and exhibits proton conductivity under high humidity.[27–30] We demonstrated that PWA enhances the PEC response in gas-fed PEC systems under UV and visible light.

Experimental

Preparation of the porous WO_3 photoanodes

The porous WO_3 photoanode was prepared by using Ti fibre felt (Nikko Techno), which served as a gas-diffusion conductive substrate (Fig. 1a).[24,31] The Ti felt was dipped in an aqueous solution of $(NH_4)_6H_2W_{12}O_{40}$ (Nippon inorganic color & chemical) and polyethylene glycol 20 000 (Fujifilm Wako pure chemical) for 30 min. The dip-coated felt was then dried at 80 °C. This treatment was repeated three times. The obtained samples were then calcined at 650 °C in air for 2 h.

The porous WO_3 electrodes were functionalized with solutions of 5 wt% Nafion PESA ionomer (D520, fuel cell store) or $H_3(PW_{12}O_{40}) \cdot nH_2O$ (Fujifilm Wako pure chemicals) by drop casting. After applying 3.5–10 μL cm^{-2} onto the surface, the drop-cast electrode was dried at 80 °C for 10 min. Subsequently, another cast was applied on the opposite side of the electrode and dried in the same manner. The loading weights of the surface electrolyte relative to WO_3 (8 mg cm^{-2}) are 12 wt% and 2–20 wt% for PFSA/WO_3 and PWA/WO_3, respectively.

Characterization

X-ray diffraction patterns were recorded on a SmartLab diffractometer (Rigaku) using Cu Kα radiation. Micro-Raman spectra were recorded on an inVia Reflex (Renishaw) with a 532-nm green laser. Surface composition was analyzed using a JSM-7800F field-emission scanning electron microscope (JEOL) with an energy-dispersive X-ray spectrometer (EDS).

PEM-PEC reaction in the gas phase

The PEC measurements were performed in a two-electrode system using a HZ-Pro S4 workstation (Hokuto Denko). The cathode was composed of a ~50 wt% Pt-loaded carbon black (Pt–CB, Tanaka Kikinzoku Kogyo) catalyst with an ionomer and Toray carbon paper (fuel cell store). A Nafion N117 film (Chemours) was sandwiched between the porous photoanode and cathode electrocatalyst by pressing at 140 °C for 4 min.

The PEC reaction was performed at 26 °C and a pressure of 1 bar. The gas flow rate was controlled using mass-flow controllers. The photoanode side was supplied with 20 mL min^{-1} of high-purity CH_4 (Osaka gas liquid, >99.999%), which was passed through the liquid water at 24 °C. The water vapour pressure was monitored using a dew point meter, EE33 (Tekhne). The relative humidity (RH) in the reactor was 80–90%, without liquid condensation. The cathode side was supplied with 20 mL min^{-1} of humidified Ar gas. The geometric surface area of the two electrodes was 4 cm^2, and that of the photoanode was 2 cm^2. Photoirradiation was performed using a 365-nm UV LED (Nitride semiconductor), and a 453-nm blue LED (OptoSupply). The incident photon-to-current conversion efficiency (IPCE) was calculated using the following equation:

$$\text{IPCE} = \frac{1240 j_{\text{photo}}}{\lambda I_0} \times 100\%,$$

where j_{photo} is the photocurrent density, λ is the wavelength (nm), and I_0 is the intensity of the incident light.

The gas products were analyzed using gas chromatography. H_2 and O_2 were quantified using a GC-8A (Shimadzu) instrument equipped with a molecular sieve 5A and a thermal conductivity detector in an Ar carrier. To quantify CO and CO_2, a He carrier was used in a Shincarbon ST column. Hydrocarbons were analyzed using a GC-2014 (Shimadzu) equipped with a GS-CarbonPLOT column, an N_2 carrier, and a flame ionization detector. The C_2H_6 selectivity on a carbon basis was calculated from the production rate of each carbon-containing product (r_i) as follows:

$$S_{C_2H_6} = \frac{2r_{C_2H_6}}{r_{CO_2} + r_{CO} + 2r_{C_2H_6}} \times 100\%$$

The C_2H_6 Faradaic efficiency (FE) value was calculated from the Faradaic constant (F) as follows:

$$\text{FE} = \frac{2F r_{C_2H_6}}{j_{\text{photo}}} \times 100\%$$

Results and discussion

The crystal structure of $H_3PW_{12}O_{40} \cdot nH_2O$ varies depending on the hydration number ($n = 6$, 14, and 21).[32] An edge-shared WO_6 shell enclosing the tetrahedrally coordinated phosphorus core,
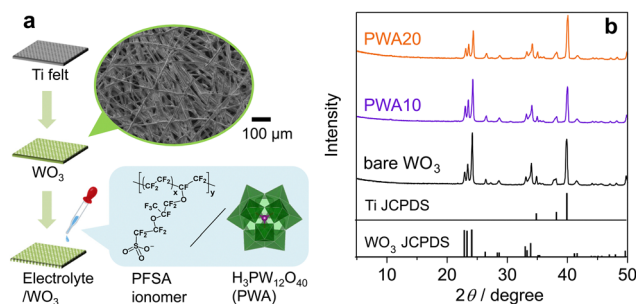

Fig. 1 (a) Preparation of porous WO_3 photoanode and surface electrolyte coating. (b) XRD patterns of PWA/WO_3 photoanodes and the standard lines of WO_3 (JCPDS No. 01-072-0677) and Ti (JCPDS No. 00-044-1294).

which is Keggin's anion unit ($PW_{12}O_{40}^{3-}$), is surrounded by protonated water layers. XRD analysis revealed no peaks attributed to $H_3PW_{12}O_{40} \cdot nH_2O$ on the PWA/WO_3 photoanodes (Fig. 1b), indicating the high dispersion of $H_3PW_{12}O_{40}$ on the porous WO_3 photoanode. All the peaks were attributed to monoclinic WO_3 and hexagonal Ti from the felt substrate. The Raman spectra of the PWA/WO_3 electrode exhibited small bands of $H_3PW_{12}O_{40}$ at 1011 and 993 cm^{-1} (Fig. 2), which are assigned to the symmetric and asymmetric stretching of the terminal W=O bond of the Keggin's unit, respectively.[33] The other Raman bands are attributed to monoclinic WO_3.[34] The XRD and Raman results indicate that $H_3PW_{12}O_{40}$ is deposited on the WO_3 surface in a highly dispersed state. The SEM observation supports the dispersed state of PWA on the WO_3 particles (Fig. S1 in ESI†).

The functionalized WO_3 photoanode and Pt–CB were attached to both sides of an N117 membrane and the prepared membrane electrode assembly was installed in a planar-type stainless-steel reactor with a glass window for irradiation (Fig. 3). The PEM-PEC measurements were performed in a two-electrode system, but the cathode potential is likely close to that of the reversible hydrogen electrode (RHE) because the overpotential for the hydrogen evolution reaction was very small over the Pt–CB electrocatalyst (Fig. S2, ESI†).

Fig. 4a shows the chronoamperometric data of the PEM-PEC system at a constant bias of 1.2 V under 365-nm UV irradiation (area 2 cm^2). The WO_3 photoanodes were employed in a continuous Ar flow with ~3 kPa of water vapour at 26 °C (RH 90%). Humidified Ar flowed into the cathode side. Under this vapour-fed condition (RH 90%), the photocurrent response was negligibly small for the bare WO_3 photoanode without a surface electrolyte because proton transfer and transport were sluggish in the absence of a liquid electrolyte. In contrast, surface coating by the Nafion ionomer significantly increased the photocurrent response under vapour-fed conditions. PWA coating also enhanced the vapour-fed PEC performance of WO_3 photoanodes. The photocurrent response of PWA/WO_3 increased with increasing PWA loading from 2 to 5 wt%. The photocurrents were stable after a steep decay during the initial 10 min. The IPCE was calculated from the steady-state photocurrent density. The IPCE values of PWA/WO_3 were maximized
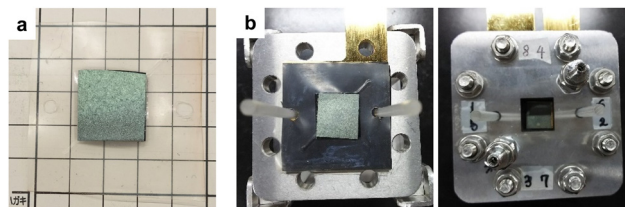

Fig. 3 (a) Membrane electrode assembly composed of the WO_3 photoanode, N117, and the Pt–CB electrocatalyst. (b) Planar-type stainless steel cell for gas-fed PEC reaction with an irradiation window of 2 cm^2.
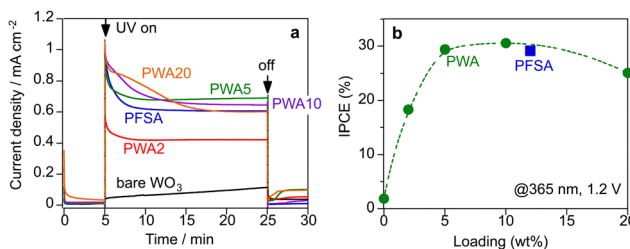

Fig. 4 Photocurrent response of the WO_3 photoanodes in a continuous flow of humidified argon (RH < 90%) under UV irradiation (365 nm, 7.0 mW cm^{-2}, area 2 cm^2). (a) Photocurrent response of WO_3 photoanodes coated with PFSA and PWA with different loading amount (wt%) at 1.2 V vs. Pt–CB cathode. (b) Incident photon-to-current conversion efficiency (IPCE) at 1.2 V.

at 5–10 wt% loading and decreased slightly at 20 wt% loading (Fig. 4b). At 365 nm, the IPCE of PWA/WO_3 was 29%, which was nearly identical to the values obtained for WO_3 in a liquid electrolyte (0.1 M H_2SO_4) at a potential of 1.2 V vs. RHE. Similar IPCE values have been reported for WO_3 photoanodes in conventional liquid electrolytes.[31,35–37] There was no significant difference in IPCE values between PWA/WO_3 and PFSA/WO_3 under vapour feeding. This indicates that the PWA acts as a surface electrolyte like PFSA ionomer for the vapour-fed condition.

Fig. 5a–c show the effect of applied voltage on the photocurrent response in the PEM-PEC system under visible light (453 nm). Initial decays of the photocurrent were significant when the applied potential was lower than 1.2 V (vs. cathode) for both PWA/WO_3 and PFSA/WO_3 photoanodes. The photocurrent response at the steady state was diminished below 0.6 V (vs. cathode). This result is consistent with the reported flat band potentials (0.3–0.5 V vs. RHE) for WO_3 electrodes.[35,38] There was no significant difference between PWA/WO_3 and PFSA/WO_3 on the applied voltage dependence. These results suggest that the charge separation efficiency is decreased when the potential drop in band bending is decreased at the steady state.

We found that the polyoxometalate loaded on the porous WO_3 photoanode acted as a surface electrolyte like PFSA ionomer with proton conductivity. Fig. 5d illustrates the role of PWA in the PEC reaction in the presence of saturated water vapour. In PEC water oxidation, the photogenerated holes promote the oxygen evolution reaction ($2H_2O \rightarrow O_2 + 4H^+ + 4e^-$) probably through the PCET process. Photoexcited electrons are
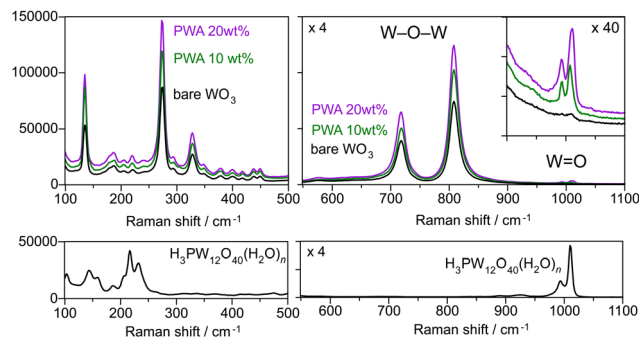

Fig. 2 Raman spectra of the WO_3 photoanodes with and without the PWA (10 and 20 wt%) coating and $H_3PW_{12}O_{40} \cdot nH_2O$ crystalline powder.
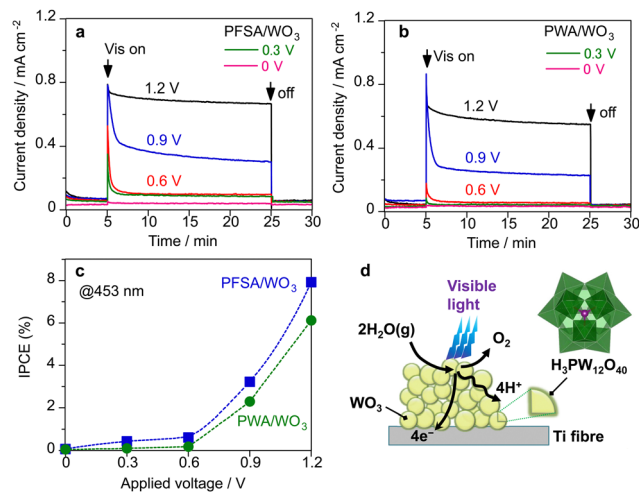
Fig. 5 Effect of applied voltage (V vs. Pt–CB cathode) on the photocurrent response of (a) PFSA/WO$_3$ and (b) PWA/WO$_3$ in the vapour-fed PEM-PEC system under visible light (453 nm, 22 mW cm^{-2}). (c) Steady-state IPCE at 453 nm after 20 min of photoirradiation. (d) Schematic illustration of PEC triple-phase boundary over the PWA/WO$_3$ photoanode. The loading of PWA and PFSA were 5 and 12 wt% relative to WO$_3$.

transported toward the conductive Ti-fibre substrate through the semiconductor particles. In conventional liquid systems, aqueous electrolytes promote proton transfer/transport in the microenvironment of photoanode materials. In contrast, the absence of aqueous electrolytes causes proton transfer and transport to be the rate-determining steps in OER. Therefore, the PFSA ionomer is required as a surface electrolyte to promote proton transfer and transport under vapour-fed conditions.

Fig. 6 shows the nitrogen and water vapour adsorption/desorption isotherms of the WO$_3$ electrodes. The BET specific surface area of bare WO$_3$, PWA/WO$_3$, and PFSA/WO$_3$ layers on Ti felt was estimated from the nitrogen adsorption to be 3.6, 2.9, and 2.6 m^2 g^{-1}, respectively. The coating of the surface electrolyte slightly reduces the specific surface area of the WO$_3$ particles. In the PEM-PEC cell, one of the roles of PFSA ionomers is considered to be capturing humidity from the moisture air to supply enough water on the photoelectrodes.[16,22] As shown in the water vapour adsorption/desorption isotherms, the PFSA/WO$_3$
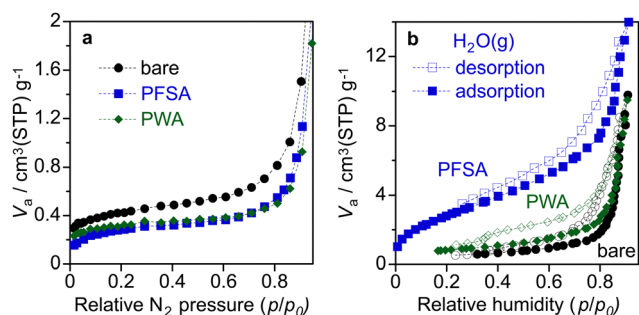
exhibits larger water uptake than those of bare WO$_3$ and PWA/WO$_3$. The water uptake of the WO$_3$ electrode was slightly increased by the loading of PWA, but the effect was not significant at higher RH regions ($p/p_0 > 0.8$). This result demonstrates that the activity enhanced by PWA is attributable to the proton transport property rather than the capture of the water vapour from humidity.

The long-term stability of the PEM-PEC cells with PFSA/WO$_3$ and PWA/WO$_3$ was tested at 1.2 V under 453 nm visible light irradiation (area 16 cm^2). Fig. 7 shows the time course of the current density and production rates in the cathode and photoanode compartments in the vapour-fed PEC water splitting. The photocurrent and production rate of PFSA/WO$_3$ gradually decreased, but was relatively stable for PWA/WO$_3$. After 20 h of photoirradiation, dark current was significantly increased for PFSA/WO$_3$. The IPCE value was calculated from the photocurrent density after subtraction of the dark current density when turning off the light. The IPCE of the PWA/WO$_3$ photoanode (2.8%) was higher than that of the PFSA/WO$_3$ photoanode (2.4%) at the 20-h PEC reaction. To further investigate the durability of the photoanodes, we compared the voltammograms before and after long-term PEC reactions (Fig. 7c and f). The photocurrent response of the PFSA/WO$_3$ photoanode was decreased after the stability test, but a significant difference was not observed for PWA/WO$_3$ between the fresh and the used photoanodes. These results indicated that stable water splitting was achieved by the PEM-PEC system using H$_3$PW$_{12}$O$_{40}$ as an inorganic solid electrolyte.

The H$_2$ FE was close to 100% on the cathode side. In contrast, the O$_2$ FE was less than 100% probably owing to CO$_2$ formation and dark current (Table S1 in ESI†). However, PWA/WO$_3$ showed an O$_2$ FE of 95%, which was significantly higher than that of PFSA/WO$_3$ (O$_2$ FE of 85%). Continuous CO$_2$ evolution during PEC reactions was observed only for the PFSA/WO$_3$ photoanode. This CO$_2$ production leading to lower O$_2$ FE is assigned to the oxidative decomposition of PFSA ionomer and membrane.[15,16]

The SEM-EDS analysis revealed that the fluorine content of the PFSA/WO$_3$ photoanode decreased from 36.5 to 18.5 mass% after the PEC reaction (Table S2, ESI†). Therefore, the CO$_2$ production primarily originated from the degradation of the PFSA ionomer coated on the photoanodes. In contrast, the P content (0.3 mass%) did not change during the PEC reaction for the PWA/WO$_3$ photoanode. The phosphorus emission mapping image revealed that the high dispersion of H$_3$PW$_{12}$O$_{40}$ on the porous WO$_3$ electrode was maintained even after the reaction (Fig. S3, ESI†). Raman spectra also confirmed the presence of two bands of H$_3$PW$_{12}$O$_{40}$ even after the vapour-fed PEC reaction (Fig. S4, ESI†). The long-term stability test was also performed under 385 nm UV light (irradiance 60 mW cm^{-2}, area 2 cm^2, Fig. S5, ESI†). After 20 h of reaction, the IPCE of the WO$_3$/PWA photoanode (2.4%) was significantly higher than that of the WO$_3$/Nafion photoanode (0.9%).

Finally, we employed the PEM-PEC cell for methane conversion reaction under visible light irradiation. Fig. 8 depicts the time course of PEC methane conversion at 1.2 V (vs. cathode).

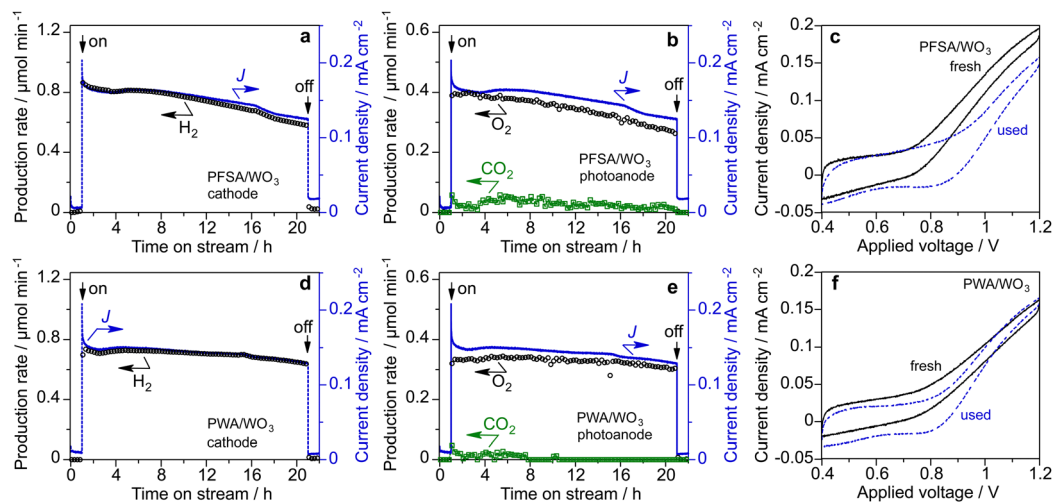**Fig. 6** (a) Nitrogen adsorption isotherms at −196 °C and (b) water vapour adsorption–desorption isotherms at 25 °C for bare WO$_3$, PWA/WO$_3$, and PFSA/WO$_3$ layers on Ti felt. The loading of PWA and PFSA were 5 and 12 wt% relative to WO$_3$.

Fig. 7 Long-term stability test of (a)–(c) PFSA/WO$_3$ and (d)–(f) PWA/WO$_3$ photoanodes in the vapour-fed PEM-PEC system under visible light (453 nm, 12 mW cm^{-2}, area 16 cm^2) at 1.2 V (vs. Pt–CB): (a) and (d) Production rate of H$_2$ in the cathode side, (b) and (e) production rate of O$_2$ and CO$_2$ in the photoanode side, and (c) and (f) cyclic voltammograms before and after the stability test.

CH$_4$ gas containing water vapour (90% RH) was continuously fed over the WO$_3$ photoanodes. The H$_2$ FE on the cathode side was approximately 100% (Table S3, ESI†). O$_2$, CO$_2$, CO, and C$_2$H$_6$ were formed on the photoanode side. The rate of O$_2$ evolution was markedly reduced by the PWA coating, which enhanced the synthesis of CO$_x$ and C$_2$H$_6$, as opposed to the PFSA ionomer coating (12 wt%). This suggests that CH$_4$ oxidation is more plausible for the PWA/WO$_3$ than for OER by water splitting. For PWA/WO$_3$, the FEs of CO$_2$, CO, and C$_2$H$_6$ were 71.3%, 9.2%, and 10.5%, respectively (Table S3, ESI†). The increased CO$_x$ formation rate implies that steam reforming of methane (CH$_4$ + xH$_2$O → CO$_x$ + (2 + x)H$_2$) is promoted even at 25 °C.[24,25,39] C$_2$H$_6$ is formed by CH$_4$ activation, implying the formation of methyl radicals and their coupling reaction.[40–43] The activation of the C–H bond of CH$_4$ is believed to be promoted by photogenerated holes and hydroxyl radicals.[24,44–47]

Conclusions

We found that phosphotungstic acid can function as a novel surface solid electrolyte for WO$_3$ photoanodes in gas-phase PEM-PEC reactions. The H$_3$PW$_{12}$O$_{40}$/WO$_3$ photoanode exhibits a photocurrent efficiency as high as that of the porous WO$_3$ photoanode functionalized by PFSA ionomer. The enhanced activity by phosphotungstic acid functionalization is attributed to the proton transport property rather than the water uptake from humidity. In the vapour-fed water-splitting reaction, the H$_3$PW$_{12}$O$_{40}$/WO$_3$ photoanode, composed of inorganic materials, was more stable than the photoanode using the organic PFSA ionomer. The H$_3$PW$_{12}$O$_{40}$ surface electrolyte was also applied for the gas-phase PEC conversion of methane to ethane and carbon oxides. This study sheds light on the use of surface inorganic electrolytes to develop robust PEM-PEC systems for converting gaseous molecules in the absence of liquid electrolytes.

Author contributions

F. Amano: conceptualization, methodology, writing; K. Tsushiro and C. Akamoto: investigation.

Conflicts of interest

There are no conflicts to declare.
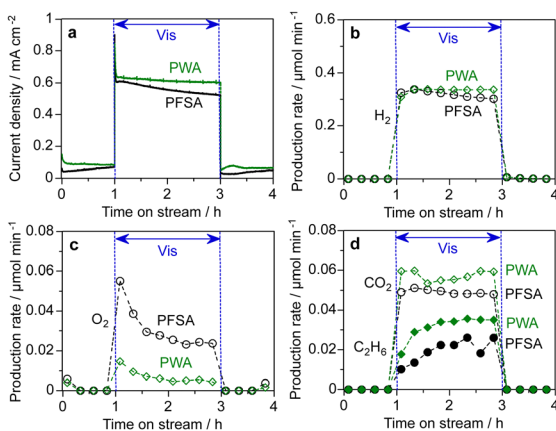
Acknowledgements

Fig. 8 PEM-PEC methane conversion reactions using the PWA/WO$_3$ and PFSA/WO$_3$ photoanodes at 1.2 V (vs. Pt–CB) under visible light irradiation (453 nm, 22 mW cm^{-2}, and area 2 cm^2): (a) photocurrent response, (b) H$_2$ production rate at the cathode, (c) O$_2$ production rate at the photoanode and (d) production rate of CO$_2$ and C$_2$H$_6$ at the photoanode.

Notes and references

1 J. I. Guo, Y. C. Zhang, A. Zavabeti, K. F. Chen, Y. L. Guo, G. P. Hu, X. L. Fan and G. K. Li, *Nat. Commun.*, 2022, **13**, 5046.

2 T. Suguro, F. Kishimoto and K. Takanabe, *Energy Fuels*, 2022, **36**, 8978–8994.

3 T. Suguro, F. Kishimoto, N. Kariya, T. Fukui, M. Nakabayashi, N. Shibata, T. Takata, K. Domen and K. Takanabe, *Nat. Commun.*, 2022, **13**, 5698.

4 J. M. Spurgeon and N. S. Lewis, *Energy Environ. Sci.*, 2011, **4**, 2993–2998.

5 C. Xiang, Y. Chen and N. S. Lewis, *Energy Environ. Sci.*, 2013, **6**, 3713–3721.

6 S. Kumari, R. T. White, B. Kumar and J. M. Spurgeon, *Energy Environ. Sci.*, 2016, **9**, 1725–1733.

7 B. Seger and P. V. Kamat, *J. Phys. Chem. C*, 2009, **113**, 18946–18952.

8 J. Georgieva, S. Armyanov, I. Poulios and S. Sotiropoulos, *Electrochem. Commun.*, 2009, **11**, 1643–1646.

9 J. Georgieva, S. Armyanov, I. Poulios, A. D. Jannakoudakis and S. Sotiropoulos, *Electrochem. Solid-State Lett.*, 2010, **13**, P11–P13.

10 K. O. Iwu, A. Galeckas, A. Y. Kuznetsov and T. Norby, *Electrochim. Acta*, 2013, **97**, 320–325.

11 J. Rongé, D. Nijs, S. Kerkhofs, K. Masschaele and J. A. Martens, *Phys. Chem. Chem. Phys.*, 2013, **15**, 9315–9325.

12 J. Rongé, S. Deng, S. Pulinthanathu Sree, T. Bosserez, S. W. Verbruggen, N. Kumar Singh, J. Dendooven, M. B. J. Roeffaers, F. Taulelle, M. De Volder, C. Detavernier and J. A. Martens, *RSC Adv.*, 2014, **4**, 29286–29290.

13 F. Amano, A. Shintani, H. Mukohara, Y. M. Hwang and K. Tsurui, *Front. Chem.*, 2018, **6**, 598.

14 F. Amano, H. Mukohara, A. Shintani and K. Tsurui, *ChemSusChem*, 2019, **12**, 1925–1930.

15 F. Amano, H. Mukohara, H. Sato and T. Ohno, *Sustainable Energy Fuels*, 2019, **3**, 2048–2055.

16 F. Amano, H. Mukohara, H. Sato, C. Tateishi, H. Sato and T. Sugimoto, *Sustainable Energy Fuels*, 2020, **4**, 1443–1453.

17 C. X. M. Ta, C. Akamoto, Y. Furusho and F. Amano, *ACS Sustainable Chem. Eng.*, 2020, **8**, 9456–9463.

18 T. Stoll, G. Zafeiropoulos and M. N. Tsampas, *Int. J. Hydrogen Energy*, 2016, **41**, 17807–17817.

19 K. Xu, A. Chatzitakis, E. Vollestad, Q. Ruan, J. Tang and T. Norby, *Int. J. Hydrogen Energy*, 2019, **44**, 587–593.

20 X. L. Kang, L. Chaperman, A. Galeckas, S. Ammar, F. Mammeri, T. Norby and A. Chatzitakis, *ACS Appl. Mater. Interfaces*, 2021, **13**, 46875–46885.

21 M. Caretti, E. Mensi, K. Raluca-Ana, L. Lazouni, B. Goldman, L. Carbone, S. Nussbaum, R. A. Wells, H. Johnson, E. Rideau, J. H. Yum and K. Sivula, *Adv. Mater.*, 2023, **35**, 2208740.

22 G. Zafeiropoulos, H. Johnson, S. Kinge, M. C. M. van de Sanden and M. N. Tsampas, *ACS Appl. Mater. Interfaces*, 2019, **11**, 41267–41280.

23 G. Zafeiropoulos, P. Varadhan, H. Johnson, L. Kamphuis, A. Pandiyan, S. Kinge, M. C. M. van de Sanden and M. N. Tsampas, *ACS Appl. Energy Mater.*, 2021, **4**, 9600–9610.

24 F. Amano, A. Shintani, K. Tsurui, H. Mukohara, T. Ohno and S. Takenaka, *ACS Energy Lett.*, 2019, **4**, 502–507.

25 F. Amano, A. Shintani, T. Sakakura, Y. Takatsuji and T. Haruyama, *Catal. Sci. Technol.*, 2023, **13**, 4640–4645.

26 L. Ghassemzadeh, K. D. Kreuer, J. Maier and K. Müller, *J. Power Sources*, 2011, **196**, 2490–2497.

27 N. Osamu, K. Teruo, O. Isao and M. Yoshizo, *Chem. Lett.*, 1979, 17–18.

28 P. Staiti, S. Freni and S. Hocevar, *J. Power Sources*, 1999, **79**, 250–255.

29 T. Kukino, R. Kikuchi, T. Takeguchi, T. Matsui and K. Eguchi, *Solid State Ionics*, 2005, **176**, 1845–1848.

30 M. Yamada and I. Honma, *J. Phys. Chem. B*, 2006, **110**, 20486–20490.

31 F. Amano, A. Shintani, K. Tsurui and Y.-M. Hwang, *Mater. Lett.*, 2017, **199**, 68–71.

32 U. B. Mioč, M. R. Todorović, M. Davidović, P. Colomban and I. Holclajtner-Antunović, *Solid State Ionics*, 2005, **176**, 3005–3017.

33 C. Rocchiccioli-Deltcheff, M. Fournier, R. Franck and R. Thouvenot, *Inorg. Chem.*, 1983, **22**, 207–216.

34 A. G. Souza-Filho, V. N. Freire, J. M. Sasaki, J. Mendes Filho, J. F. Julião and U. U. Gomes, *J. Raman Spectrosc.*, 2000, **31**, 451–454.

35 C. Santato, M. Ulmann and J. Augustynski, *J. Phys. Chem. B*, 2001, **105**, 936–940.

36 F. Amano, M. Tian, G. Wu, B. Ohtani and A. Chen, *ACS Appl. Mater. Interfaces*, 2011, **3**, 4047–4052.

37 H. Homura, B. Ohtani and R. Abe, *Chem. Lett.*, 2014, **43**, 1195–1197.

38 F. Amano, M. Tian, B. Ohtani and A. Chen, *J. Solid State Electrochem.*, 2012, **16**, 1965–1973.

39 W. Li, D. He, G. Hu, X. Li, G. Banerjee, J. Li, S. H. Lee, Q. Dong, T. Gao, G. W. Brudvig, M. M. Waegele, D.-e Jiang and D. Wang, *ACS Cent. Sci.*, 2018, **4**, 631–637.

40 B. Kraeutler and A. J. Bard, *J. Am. Chem. Soc.*, 1977, **99**, 7729–7731.

41 B. Kraeutler, C. D. Jaeger and A. J. Bard, *J. Am. Chem. Soc.*, 1978, **100**, 4903–4905.

42 S. Sato, *J. Phys. Chem.*, 1983, **87**, 3531–3537.

43 T. Sakata, T. Kawai and K. Hashimoto, *J. Phys. Chem.*, 1984, **88**, 2344–2350.

44 H. Tateno, S. Iguchi, Y. Miseki and K. Sayama, *Angew. Chem., Int. Ed.*, 2018, **57**, 11238–11241.

45 J. Ma, K. K. Mao, J. X. Low, Z. H. Wang, D. W. Xi, W. Q. Zhang, H. X. Ju, Z. M. Qi, R. Long, X. J. Wu, L. Song and Y. J. Xiong, *Angew. Chem., Int. Ed.*, 2021, **60**, 9357–9361.

46 A. Mehmood, S. Y. Chae and E. D. Park, *Catalysts*, 2021, **11**, 1387.

47 F. Amano and M. Ishimaru, *Energy Fuels*, 2022, **36**, 5393–5402.